

Thin Accretion Disk onto slowly rotating black holes in Einstein-Æther theory

Cheng Liu^{a,b,*}, Sen Yang^{a,b,c,†}, Qiang Wu^{a,b,‡} and Tao Zhu^{a,b,§}

^a*Institute for Theoretical Physics & Cosmology, Zhejiang University of Technology, Hangzhou, 310023, China*

^b*United Center for Gravitational Wave Physics (UCGWP),
Zhejiang University of Technology, Hangzhou, 310023, China*

^c*Institute of theoretical physics, Lanzhou University, Lanzhou 730000, China*

(Dated: March 17, 2022)

The accretion disk is formed by particles moving in closed orbits around a compact object, whose physical properties and the electromagnetic radiation characteristics are determined by the space-time geometry around the compact object. In this paper, we study the physical properties and the optical appearance of the electromagnetic radiation emitted from a thin accretion disk around the two types of the black hole solution in Einstein-Æther theory. We investigate in detail the effects of the æther field on the energy flux, temperature distribution, and electromagnetic spectrum of the disk in the two types of slowly rotating Einstein-Æther black holes. Then we plot the ray-traced redshifted image as well as the intensity and polarization profile of a lensed accretion disk around the two types of Einstein-Æther black holes. We found that from the image simulation, the æther field only has a certain effect on the central shadow area of the accretion disk.

I. INTRODUCTION

Black holes are some of the most extreme objects as a direct inference of the General Relativity (GR). So far, black holes are the strongest gravitational field sources known in our universe, with a pretty high spin and high-intensity magnetic field as usual. These properties make black holes outstanding laboratories to study both matter and gravity in situations out of reach in terrestrial and astrophysics experiments. Their existence as physical objects has become our consensus due to a series of available observations, such as gravitational waves generated due to the merging of black holes observed by the LIGO & Virgo collaboration experiment [1], the extraordinary observation of the M87* black hole shadow by the Event Horizon Collaboration [2–7], and the observations of the electromagnetic spectrum emitted from an accretion disk around a black hole [8–10].

An accretion disk is a flattened structure formed by rotating magnetofluid which slowly spirals into a compact central objects. A fraction of the heat, which from the gravitational energy released by the magnetofluid, is converted to radiation which is emitted from the inner part of the accretion disk. When these emitted radiation reaches X-ray, optical or radio astronomy telescopes, it provides the possibility of analyzing its electromagnetic spectrum. With these observations of black holes in gravitational and electromagnetic spectra, together with their future developments, such as the Next Generation Very Large Array [11], the Thirty Meter Telescope [12], and the BlackHoleCam [13], tests of GR and its alternatives in the strong gravity regime are a hot topic nowadays.

The standard model of geometrically thin and optically thick accretion disk was first proposed by Shakura and Sunyaev in 1973 [14]. Then it was developed by Novikov and Thorne [15], and Page and Thorne [16], and has been successfully applied to astrophysical black hole candidates to explain the features of their observed spectra for many years.

On the other hand, the experimental verification of symmetry breaking is one of the most powerful tools to understand in which direction to extend the current canon toward more fundamental physical theories. The Lorentz invariance is one of the fundamental principles of GR. However, when one considers the quantization of the gravity, such invariance could be violated in the high-energy regime. In this sense, the Lorentz symmetry can only be treated as an approximate symmetry, which emerges at low energies and is violated at higher energies. With these thoughts, a lot of modified gravity theories have been proposed, such as the Horava-Lifshitz theories of quantum gravity [17–20] and Einstein-Æther theory [21–25].

Einstein-Æther gravitational theory is a modification of Einstein's General Relativity where the kinematic quantities of a unitary time-like vector field, known as æther, is introduced in the gravitational action [21–25]. One of the important characteristics of the Einstein-Æther theory is that it describes the classical limit of Hořava gravity [17, 18]. The presence of the æther field defines a preferred timelike direction that violates the Lorentz symmetry [26, 27]. The breaking of Lorentz symmetry might occur at the Planck or quantum gravity scales if the spacetime continuum is reduced to a discrete structure, thereby causing spacetime to be an emergent phenomenon. Therefore, it is of great interesting to explore the properties of the accretion disk around black holes with the presence of the æther field.

Not so long ago, two static, charged, and spherically symmetric black hole solutions have been found in the Einstein-Æther theory with two specific combinations of

* liucheng@zjut.edu.cn

† yangs19@lzu.edu.cn

‡ wuq@zjut.edu.cn

§ zhut05@zjut.edu.cn; Corresponding author

the coupling constants [27]. Another spherically symmetric black hole solution for a class of coupling constants has also been explored by using numerical calculation, and its analytical representation in the polynomial form has been used in the study of the quasinormal modes in the Einstein-Æther theory [28–32]. With these spherically symmetric black hole solutions, one can apply the procedure in Refs. [33] to generate the slowly rotating black hole solutions, which has been used in the study of the black holes shadow cast in the Einstein-Æther theory [34]. These solutions, which contain the effects of the æther field, can be used to investigate the effects of the æther field in the accretion disk and compare with the results of GR.

The aim of our work is to study a geometrically thin and optically thick accretion disk around a charged and slowly rotating black hole in Einstein-Æther theory. For an astrophysical black hole, the study of the electromagnetic spectrum from the accretion process around the black hole is a powerful approach to explore the nature of the black hole spacetime in the regime of strong gravity. This has stimulated a lot works on the studies of the thin accretion disk around various black hole spacetimes, see [35–49, 51–64] and references therein. Therefore, it is natural to ask whether the æther field corrections of the Einstein-Æther theory can appear in the electromagnetic signatures and the optical appearance to a distant observer of the accretion disk. To answer this question, we consider a thin relativistic accretion disk model around the charged and slowly rotating Einstein-Æther black hole, which is in a steady-state and in hydrodynamic and thermodynamic equilibrium. In particular, we calculate the energy flux, temperature distribution, and electromagnetic spectrum of the thin accretion disk, and compare them with the standard GR case. Meanwhile, we have analyzed the observable images of the thin accretion disk in its vicinity and the radiation emitted by it, and compared the possible deviation from the case of the Schwarzschild black hole. The possible effects of the æther field corrections on the electromagnetic signatures from the thin accretion disk are also explored.

The content of our paper is as follows. In Sec. II, we present a brief review of the charged and slowly rotating black hole solutions and their properties in the Einstein-Æther theory. Then with this rotating solution, we study the geodesic and the radius of the marginally stable circular orbit vary with the æther field coupling parameter c_{13} and c_{14} in Sec. III. In Sec. IV, we study the properties of the thin accretion disk onto the charged and slowly rotating black hole in Einstein-Æther theory and discuss the flux energy of the accretion disk with the effect from æther field. In Sec. V, we present the Ray-traced redshifted image and intensity and polarization profile of a lensed accretion disk around the two classes of black holes solution in Einstein-Æther theory considered here, and we comment on the novel features that we obtain by our analysis. The summary and discussion for this paper is presented in Sec. VI.

II. BLACK HOLE SOLUTIONS IN EINSTEIN-ÆTHER THEORY

In this section, we review briefly the black hole solutions in the Einstein-Æther theory focusing on its analytic case. Einstein-Æther theory is essentially general relativity (GR) coupled with a unit, timelike vector field, u^μ . The unit and timelike properties of the æther field forces it to be ever-present, even in the local frame, thus selecting a preferred time direction and violating the local Lorentz symmetry. The action for the Æther theory makes all possible terms that are quadratic in the first derivatives of u^μ . So the Einstein-Æther theory can be considered as an effective description of Lorentz symmetry breaking in the gravity sector. Otherwise, it has been extensively used in order to obtain quantitative constraints on Lorentz-violating gravity.

With the unit and timelike vector, the general action of the Einstein-Æther theory is given by [23]

$$S_{\text{æ}} = \frac{1}{16\pi G_{\text{æ}}} \int d^4x \sqrt{-g} (R + \mathcal{L}_{\text{æ}}), \quad (2.1)$$

where g is the determinant of the four dimensional metric $g_{\mu\nu}$ of the space-time with the signatures $(-, +, +, +)$, R is the Ricci scalar, $G_{\text{æ}}$ is the æther gravitational constant, and the Lagrangian of the æther field $\mathcal{L}_{\text{æ}}$ is given by

$$\mathcal{L}_{\text{æ}} \equiv -M^{\alpha\beta}{}_{\mu\nu} (D_\alpha u^\mu) (D_\beta u^\nu) + \lambda (g_{\mu\nu} u^\mu u^\nu + 1). \quad (2.2)$$

Here D_α denotes the covariant derivative with respect to $g_{\mu\nu}$, λ is a Lagrangian multiplier, which guarantees that the aether four-velocity u^α is always timelike, and $M^{\alpha\beta}{}_{\mu\nu}$ is defined as ¹

$$M^{\alpha\beta}{}_{\mu\nu} \equiv c_1 g^{\alpha\beta} g_{\mu\nu} + c_2 \delta_\mu^\alpha \delta_\nu^\beta + c_3 \delta_\nu^\alpha \delta_\mu^\beta - c_4 u^\alpha u^\beta g_{\mu\nu}. \quad (2.3)$$

The four coupling constants c_i 's are all dimensionless, and $G_{\text{æ}}$ is related to the Newtonian constant G_N via the relation [67],

$$G_{\text{æ}} = \frac{G_N}{1 - \frac{1}{2}c_{14}} \quad (2.4)$$

with $c_{14} \equiv c_1 + c_4$. In order to discuss the black hole solution with electric charge, we also add a source-free Maxwell Lagrangian \mathcal{L}_M to the theory, then the total action of the theory becomes,

$$S_{\text{æ},M} = S_{\text{æ}} + \int d^4x \sqrt{-g} \mathcal{L}_M, \quad (2.5)$$

where

$$\mathcal{L}_M = -\frac{1}{16\pi G_{\text{æ}}} F^{\mu\nu} F_{\mu\nu}, \quad (2.6)$$

¹ The parameters (c_1, c_2, c_3, c_4) used in this paper are related to parameters $(c_\theta, c_\sigma, c_\omega, c_a)$ by the relations $c_\theta = c_1 + 3c_2 + c_3$, $c_\sigma = c_1 + c_3 = c_{13}$, $c_\omega = c_1 - c_3$, $c_a = c_1 + c_4 = c_{14}$.

$$F_{\mu\nu} = D_\mu A_\nu - D_\nu A_\mu, \quad (2.7)$$

where A_μ is the electromagnetic potential four-vector. It is worth noting that the electromagnetic field A_μ is minimally coupled to the gravity and the æther field u_μ . The variations of the total action with respect to $g_{\mu\nu}$, u^α , λ , and A^a yield, respectively, the field equations,

$$E^{\mu\nu} = 0, \quad (2.8)$$

$$\mathbb{E}_\alpha = 0, \quad (2.9)$$

$$g_{\mu\nu} u^\mu u^\nu = -1, \quad (2.10)$$

$$D^\mu F_{\mu\nu} = 0. \quad (2.11)$$

where

$$E^{\mu\nu} \equiv R^{\mu\nu} - \frac{1}{2}g^{\mu\nu}R - 8\pi G_{\mathfrak{a}}T_{\mathfrak{a}}^{\mu\nu}, \quad (2.12)$$

$$\mathbb{E}_\alpha \equiv D_\mu J^\mu{}_\alpha + c_4 a_\mu D_\alpha u^\mu + \lambda u_\alpha, \quad (2.13)$$

with

$$\begin{aligned} T_{\alpha\beta}^{\mathfrak{a}} &\equiv D_\mu \left[J^\mu{}_{(\alpha} u_{\beta)} + J_{(\alpha\beta)} u^\mu - u_{(\beta} J_{\alpha)}{}^\mu \right] \\ &+ c_1 \left[(D_\alpha u_\mu) (D_\beta u^\mu) - (D_\mu u_\alpha) (D^\mu u_\beta) \right] \\ &+ c_4 a_\alpha a_\beta + \lambda u_\alpha u_\beta - \frac{1}{2} g_{\alpha\beta} J^\delta{}_\sigma D_\delta u^\sigma, \\ J^\alpha{}_\mu &\equiv M^{\alpha\beta}{}_{\mu\nu} D_\beta u^\nu, \\ a^\mu &\equiv u^\alpha D_\alpha u^\mu. \end{aligned} \quad (2.14)$$

From Eqs.(2.9) and (2.10), we find that

$$\lambda = u_\beta D_\alpha J^{\alpha\beta} + c_4 a^2, \quad (2.15)$$

where $a^2 \equiv a_\lambda a^\lambda$.

A. Static and Charged Spherically Symmetric Einstein-æther Black Holes

The general form for a static spherically symmetric metric for the Einstein-Æther black hole spacetimes can be written in the Eddington-Finkelstein coordinate system as

$$ds^2 = -e(r)dv^2 + 2f(r)dvd r + r^2(d\theta^2 + \sin^2\theta d\phi^2), \quad (2.16)$$

with the corresponding Killing vector χ^a and the æther vector field u^a being given by

$$\chi^a = (1, 0, 0, 0), \quad u^a(r) = (\alpha(r), \beta(r), 0, 0), \quad (2.17)$$

where $e(r)$, $f(r)$, $\alpha(r)$, and $\beta(r)$ are functions of r only. The boundary conditions on the metric components are such that the solution is asymptotically flat, while those for the æther components are such that

$$\lim_{r \rightarrow +\infty} u^a = (1, 0, 0, 0). \quad (2.18)$$

As shown in [27], there exist two types of exact static and charged spherically symmetric black hole solutions in Einstein-æther theory. The first solution corresponds to the special choice of coupling constants $c_{14} = 0$ and $c_{123} \neq 0$ where $c_{123} \equiv c_1 + c_2 + c_3$, while the second solution corresponds to $c_{123} = 0$.

1. $c_{14} = 0$ and $c_{123} \neq 0$

For the first solution, we have [27]

$$e(r) = 1 - \frac{2M}{r} + \frac{Q^2}{r^2} - \frac{27c_{13}}{256(1-c_{13})} \left(\frac{2M}{r} \right)^4, \quad (2.19)$$

$$f(r) = 1, \quad (2.20)$$

$$\alpha(r) = \left[\frac{1}{\sqrt{1-c_{13}}} \frac{3\sqrt{3}}{16} \left(\frac{2M}{r} \right)^2 + \sqrt{1 - \frac{2M}{r} + \frac{27}{256} \left(\frac{2M}{r} \right)^4} \right]^{-1}, \quad (2.21)$$

$$\beta(r) = -\frac{1}{\sqrt{1-c_{13}}} \frac{3\sqrt{3}}{16} \left(\frac{2M}{r} \right)^2, \quad (2.22)$$

where M and Q are the mass and the electric charge of the black hole spacetime respectively. It is obvious that when $c_{13} = 0$, the above solution reduces to the Reissner-Nordström black hole.

2. $c_{123} = 0$

For the second solution, we have [27]

$$e(r) = 1 - \frac{2M}{r} + \frac{Q^2}{(1-c_{13})r^2} - \frac{2c_{13} - c_{14}}{8(1-c_{13})} \left(\frac{2M}{r} \right)^2, \quad (2.23)$$

$$f(r) = 1, \quad (2.24)$$

$$\alpha(r) = \frac{1}{1 + \frac{1}{2} \left[\sqrt{\frac{2-c_{14}}{2(1-c_{13})}} - 1 \right] \frac{2M}{r}}, \quad (2.25)$$

$$\beta(r) = -\frac{1}{2} \sqrt{\frac{2-c_{14}}{2(1-c_{13})}} \frac{2M}{r}. \quad (2.26)$$

In this case, when $c_{13} = 0 = c_{14}$, it also reduces to the Reissner-Nordström black hole.

For both solutions, it is convenient to write the metric (2.16) in the Eddington-Finkelstein coordinate system in the form of the usual (t, r, θ, ϕ) coordinates. This can be achieved by using the coordinate transformation

$$dt = dv - \frac{dr}{e(r)}, \quad dr = dr. \quad (2.27)$$

Then the metric of the background spacetime turns into the form

$$ds^2 = -e(r)dt^2 + \frac{dr^2}{e(r)} + r^2(d\theta^2 + \sin^2\theta d\phi^2). \quad (2.28)$$

In this metric, the æther field reads

$$u^a = \left(\alpha(r) - \frac{\beta(r)}{e(r)}, \beta(r), 0, 0 \right). \quad (2.29)$$

B. Slowly rotating black holes

The rotating black hole in the slow rotation limit in general can be described by the well-known Hartle-Thorne metric [68]

$$ds^2 = -e(r)dt^2 + \frac{B(r)dr^2}{e(r)} + r^2(d\theta^2 + \sin^2\theta d\phi^2) - \epsilon r^2 \Omega(r, \theta) dt d\phi + \mathcal{O}(\epsilon^2), \quad (2.30)$$

where $e(r)$ represents the “seed” static, spherically-symmetric solutions when $\Omega(r, \theta) = 0$, ϵ denotes a small perturbative rotation parameter. For discussions of the black holes in this paper, we consider $B(r) = 1$ [33, 69]. The æther configuration in the slow-rotation limit is described by [69]

$$u_a dx^a = [\beta(r) - e(r)\alpha(r)]dt + \frac{\beta(r)}{e(r)}dr + \epsilon[\beta(r) - e(r)\alpha(r)]\lambda(r, \theta)\sin^2\theta d\phi + \mathcal{O}(\epsilon^2), \quad (2.31)$$

where $\lambda(r, \theta)$ is related to the æther’s angular momentum per unit energy by $u_\phi/u_t = \lambda(r, \theta)\sin^2\theta$.

For asymptotically flat boundary condition, as shown in [69], $\Omega(r, \theta)$ and $\lambda(r, \theta)$ have to be θ -independent, namely $\Omega(r, \theta) = \Omega(r)$ and $\lambda(r, \theta) = \lambda(r)$. Then the æther’s angular velocity can be written as

$$\psi(r) = \frac{u^\phi}{u^t} = \frac{1}{2}\Omega(r) - \frac{\lambda(r)}{r^2}. \quad (2.32)$$

The slowly rotating black holes in the Einstein-Æther theory have been obtained in [33, 69] and have been discussed in several papers that related to Horava-Lifshitz gravity [33]. While in these mentioned papers only neutral black holes have been considered, in this subsection, we present the metric of the charged slowly rotating black holes by directly applying the forms in [69] for $c_{14} = 0$ but $c_{123} \neq 0$ and $c_{123} = 0$ respectively.

1. $c_{14} = 0$ and $c_{123} \neq 0$

For this case, there exists slowly rotating black hole solution in the Einstein-Æther theory with a spherically symmetric (hypersurface-orthogonal) æther field configuration, which leads to

$$\Omega(r) = \frac{4J}{r^3} \text{ and } \lambda(r) = 0. \quad (2.33)$$

The metric now reads

$$ds^2 = -e(r)dt^2 + \frac{dr^2}{e(r)} + r^2(d\theta^2 + \sin^2\theta d\phi^2) - \frac{4M}{r}a\sin^2\theta dt d\phi + \mathcal{O}(\epsilon^2). \quad (2.34)$$

Note that $e(r)$ is given by Eq. (2.23).

2. $c_{123} = 0$

For this case, there is no closed form for the expression of $\Omega(r)$ and $\lambda(r)$ except in the limit $c_\omega = c_1 - c_3 \rightarrow \infty$. In [69], the asymptotic forms for the derivatives $\Omega'(r)$ and $\lambda'(r)$ has been obtained by expanding them for large r and the corresponding integration constants can be determined by using numerical calculation. In the limit $c_\omega \rightarrow \infty$, the frame dragging potential $\Omega(r)$ has the form [69]

$$\Omega(r) = \frac{4J}{4}. \quad (2.35)$$

Then the metric in this case takes the same form as (2.34) but with $e(r)$ given by Eq. (2.19). As pointed out in [33], the Einstein-æther theory in the limit $c_\omega \rightarrow \infty$ coincides to the non-projectable Horava-Lifshitz theory of gravity in the infrared limit, thus the solutions in the Einstein-æther theory with $c_\omega \rightarrow \infty$ are also solutions of the Horava-Lifshitz theory of gravity.

C. Numerical black hole solution

Except the black hole solutions in the analytical form, the numerical black hole solution has also been explored in the Einstein-Æther theory for a class of coupling constants [28]. For spherically symmetric solution, c_4 can be absorbed into other coupling constants. In [28], the so-called non-reduced Einstein-Æther theory is considered, for which $c_3 = 0$, and then one can use the field redefinition that fixes the coefficient c_2 [28, 31, 32],

$$c_2 = -\frac{-2c_1^3}{2 - 4c_1 + 3c_1^3}, \quad (2.36)$$

so that c_1 is the only free parameter in the numerical black hole solution in [28]. With these set-up, the metric for a spherically symmetric static black hole can still be described by (2.16), in which the functions $e(r)$, $f(r)$, $\alpha(r)$, and $\beta(r)$ are determined by numerical calculations. An approximate form of $e(r)$ and $f(r)$ are given in the polynomial form in [31, 32] as

$$e(r) = \frac{\sum_{i=0}^{N_e} a_i^{(e)} r^i}{1 + \sum_{i=0}^{N_e} b_i^{(e)} r^i}, \quad (2.37)$$

$$f(r) = \frac{\sum_{i=0}^{N_f} a_i^{(f)} r^i}{1 + \sum_{i=0}^{N_f} b_i^{(f)} r^i}, \quad (2.38)$$

where the coefficients $(a_i^{(e)}, b_i^{(e)}; a_i^{(f)}, b_i^{(f)})$ can be determined by fitting the above analytical form with numerical solutions, which is out of the scope of the current paper. The general features of the this numerical black hole has been discussed in [28, 31, 32], and it has been shown that the æther parameter c_1 trends to decrease the radius of the horizon.

In addition, Ref [29] also gives other various numerical solutions of the Einstein-Æther theory more recently, which with an accuracy that is at least two orders higher than previous ones. We will not introduce and discuss their numerical solutions in detail here.

III. THE GEODESIC OF SLOWLY ROTATING BLACK HOLES IN EINSTEIN-ÆTHER THEORY

The accretion disk is formed by particles moving in circular orbits around a compact object, whose physical properties and the electromagnetic radiation characteristics are determined by the space-time geometry around the compact object. For the purpose to study the electromagnetic properties of the thin accretion disk around a charged and slowly rotating black hole in Einstein-Æther theory, let us first consider the evolution of a massive particle in the black hole spacetime. We start with the Lagrangian of the particle,

$$L = \frac{1}{2} g_{\mu\nu} \frac{dx^\mu}{d\lambda} \frac{dx^\nu}{d\lambda}, \quad (2.39)$$

where λ denotes the affine parameter of the world line of the particle. For massless particle we have $L = 0$ and for massive one $L < 0$. Then the generalized momentum p_μ of the particle can be obtained via

$$p_\mu = \frac{\partial L}{\partial \dot{x}^\mu} = g_{\mu\nu} \dot{x}^\nu, \quad (2.40)$$

which leads to four equations of motions for a particle with energy \tilde{E} and angular momentum \tilde{L} ,

$$p_t = g_{tt}\dot{t} + g_{t\phi}\dot{\phi} = -\tilde{E}, \quad (2.41)$$

$$p_\phi = g_{\phi t}\dot{t} + g_{\phi\phi}\dot{\phi} = \tilde{L}, \quad (2.42)$$

$$p_r = g_{rr}\dot{r}, \quad (2.43)$$

$$p_\theta = g_{\theta\theta}\dot{\theta}. \quad (2.44)$$

Here a dot denotes the derivative with respect to the affine parameter λ of the geodesics. From these expressions we obtain

$$\dot{t} = \frac{g_{\phi\phi}\tilde{E} + g_{t\phi}\tilde{L}}{g_{t\phi}g_{\phi t} - g_{tt}g_{\phi\phi}} = \frac{r^4\tilde{E} - 2Mr a\tilde{L}}{4M^2a^2\sin^2\theta + r^2e(r)}, \quad (2.45)$$

$$\dot{\phi} = \frac{\tilde{E}g_{t\phi} + g_{tt}\tilde{L}}{g_{tt}g_{\phi\phi} - g_{t\phi}g_{\phi t}} = \frac{2Mar\sin^2\theta\tilde{E} + r^2e(r)\tilde{L}}{r^4e(r)\sin^2\theta + 4M^2a^2\sin^4\theta}. \quad (2.46)$$

Note that in the derivation of the above equation we have used the metric in (2.34). For timelike geodesics, we have $g_{\mu\nu}\dot{x}^\mu\dot{x}^\nu = -1$. Substituting \dot{t} and $\dot{\phi}$ we can get

$$\begin{aligned} g_{rr}\dot{r}^2 + g_{\theta\theta}\dot{\theta}^2 &= -1 - g_{tt}\dot{t}^2 - g_{\phi\phi}\dot{\phi}^2 - 2g_{t\phi}\dot{t}\dot{\phi} \\ &= -1 + \frac{r(r^3\tilde{E}^2 + 4aM\tilde{E}\tilde{L} + re(r)\tilde{L}^2\csc^2\theta)}{4a^2M^2\sin^2\theta - r^4e(r)} \end{aligned} \quad (2.47)$$

We are interested in the evolution of the particle in the equatorial circular orbits. For this reason, we can

consider $\theta = \pi/2$ and $\dot{\theta} = 0$ for simplicity. Then the above expression can be simplified into the form

$$\dot{r}^2 = V_{\text{eff}}(r, M, \tilde{E}, \tilde{L}), \quad (2.48)$$

where $V_{\text{eff}}(r)$ denotes the effective potential of the test particle with energy \tilde{E} and axial component of the angular momentum \tilde{L} , which is given by

$$V_{\text{eff}}(r) = \frac{1}{e(r)} - \frac{r^4\tilde{E}^2 + 4arM\tilde{E}\tilde{L} + r^2e(r)\tilde{L}^2}{4a^2M^2e(r) - r^4e^2(r)} \quad (2.49)$$

If we take the $e(r)$ defined by (2.23), one immediately observes that $V_{\text{eff}}(r) \rightarrow 1$ as $r \rightarrow +\infty$, as expected for an asymptotically flat spacetime. With this case, the particles with energy $\tilde{E} > 1$ can escape to infinity, and $\tilde{E} = 1$ is the critical case between bound and unbound orbits. In this sense, the maximum energy for the bound orbits is $\tilde{E} = 1$. Physically, the emergence of the coupling constant has a correction to the structure of spacetime, resulting in a change in the effective potential, naturally, as we'll discuss next, it also affects the size of the radius of the marginally stable circular orbit. The stable circular orbits in the equatorial plane are corresponding to those orbits with constant r , i.e., $\dot{r}^2 = 0$ and $dV_{\text{eff}}(r)/dr = 0$. With these conditions, one can write the specific energy \tilde{E} , the specific angular momentum \tilde{L} , and the angular velocity Ω of the particle moving in a circular orbit in the black hole as

$$\tilde{E} = -\frac{g_{tt} + g_{t\phi}\Omega}{\sqrt{-g_{tt} - 2g_{t\phi}\Omega - g_{\phi\phi}\Omega^2}}, \quad (2.50)$$

$$\tilde{L} = \frac{g_{r\phi} + g_{\phi\phi}\Omega}{\sqrt{-g_{tt} - 2g_{t\phi}\Omega - g_{\phi\phi}\Omega^2}}. \quad (2.51)$$

Since the test particles follow geodesic, equatorial, and circular orbits. We can write the geodesic equations as

$$\frac{d}{d\lambda}(g_{\mu\nu}\dot{x}^\nu) - \frac{1}{2}(\partial_\mu g_{\nu\rho})\dot{x}^\nu\dot{x}^\rho = 0, \quad (2.52)$$

with the conditions $\dot{r} = \dot{\theta} = \ddot{r} = 0$ for equatorial circular orbits, the radial component of Eq.(2.52) reduces to

$$(\partial_r g_{tt})\dot{t}^2 + 2(\partial_r g_{t\phi})\dot{t}\dot{\phi} + (\partial_r g_{\phi\phi})\dot{\phi}^2 = 0. \quad (2.53)$$

Therefore, we get the angular velocity

$$\Omega = \frac{d\phi}{dt} = \frac{-\partial_r g_{t\phi} \pm \sqrt{(\partial_r g_{t\phi})^2 - (\partial_r g_{tt})(\partial_r g_{\phi\phi})}}{\partial_r g_{\phi\phi}} \quad (2.54)$$

The marginally stable circular orbits around the slowly rotating Einstein-Æther black hole can be determined from the condition

$$d^2V_{\text{eff}}(r)/dr^2 = 0. \quad (2.55)$$

In order to conveniently characterize the influence of the æther field on the space-time around the black hole, we redefine the following two quantities

$$\kappa \equiv \frac{c_{13}}{1 - c_{13}}, \quad \varepsilon \equiv \frac{2c_{13} - c_{14}}{8(1 - c_{13})}. \quad (2.56)$$

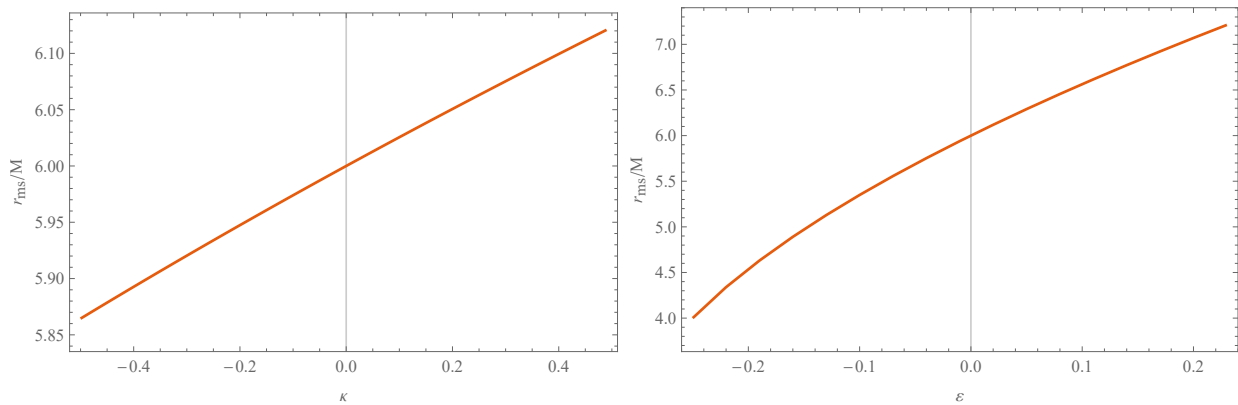


FIG. 1. Impact of the æther coupling constant κ (left panel) and ε (right panel) on the marginally stable orbit radius r_{ms} for particles moving in the thin accretion disk around the first and second Einstein-Æther black hole, respectively. Here we only considered the neutral black hole case.

They correspond to the first type solution and the second type solution in the Einstein-æther theory, respectively. Combining this equation with (2.50) and (2.51) and solving for r , the radius of the marginally stable circular orbit can be calculated numerically, which does not admit any analytical solution. We solve it numerically and plot the result in Fig. 1, which shows clearly the radius of the marginally stable circular orbit r_{ms} is increasing as the increasing of the æther field coupling constant κ for the first type Einstein-Æther black hole and ε for the second type.

In addition, we give an approximate analytic result of the marginally stable circular orbits for the first type Einstein-Æther black hole by making Taylor expansion when κ is small with $a = 0$, which is

$$r_{\text{ms}} \simeq 6M \left(1 + \frac{11M\kappa}{256} \right). \quad (2.57)$$

Similarly, we can give an approximate analytic result for the second type solution when c_{13} and c_{14} are small with $a = 0$, that is

$$r_{\text{ms}} \simeq 6M(1 + \varepsilon). \quad (2.58)$$

These approximate analytical results clearly show a key difference between the charged and slowly rotating Einstein-Æther black hole and the Schwarzschild black hole in general relativity, which is also an important physical quantity that is not difficult to observe.

IV. THE PROPERTIES OF THIN ACCRETION DISK ONTO SLOWLY ROTATING BLACK HOLES IN EINSTEIN-ÆTHER THEORY

In this section we will apply the steady-state thin accretion disk model to study the accretion process around the slowly rotating black hole in Einstein-Æther theory. As we all know, the usual astrophysical black holes are neutral, so we also choose to discuss zero charged case

here. Novikov, Thorne, and Page [15, 16] made a relativistic analysis of the structure of an accretion disk around a black hole. They assumed that the background space-time geometry was static, axisymmetric, asymptotically flat, and reflectively symmetric. They also assumed that the central plane of the disk overlapped with the equatorial plane of the black hole. This assumption leads to measure coefficient of g_{tt} , $g_{t\phi}$, g_{rr} , $g_{\theta\theta}$ and $g_{\phi\phi}$ only depends on the radial coordinates r . In this model, the stress-energy tensor of the accreting matter in the disk is decomposed according to

$$T^{\mu\nu} = \rho_0 u^\mu u^\nu + 2u^{(\mu} q^{\nu)} + t^{\mu\nu}, \quad (2.59)$$

where

$$u_\mu q^\mu = 0, \quad u_\mu t^{\mu\nu} = 0 \quad (2.60)$$

where the quantities ρ_0 , q^μ and $t^{\mu\nu}$ represents the rest mass density, the energy flow vector and the stress tensor of the accreting matter, respectively, which is defined in the averaged rest-frame of the orbiting particle with four-velocity u^μ . From the equation if the rest mass conservation, $\nabla_\mu(\rho_0 u^\mu) = 0$, it follows that the time averaged rate of the accretion of the rest mass is independent of the disk radius,

$$\begin{aligned} \dot{M}_0 &\equiv -2\pi\sqrt{-g}\Sigma u^r = \text{constant}, \\ \Sigma(r) &= \int_{-H}^H \langle \rho_0 \rangle dz. \end{aligned} \quad (2.61)$$

where $\Sigma(r)$ is the averaged rest mass density. According to the conservation law of the energy and the law of the angular momentum conservation

$$\nabla_\mu(\rho_0 u^\mu) = 0, \quad \nabla_\mu J^\mu = 0, \quad (2.62)$$

we have the integral form

$$[\dot{M}_0 \tilde{E} - 2\pi\sqrt{-g}\Omega W_\phi^r]_{,r} = 4\pi r F(r) \tilde{E}, \quad (2.63)$$

$$[\dot{M}_0 \tilde{L} - 2\pi\sqrt{-g}W_\phi^r]_{,r} = 4\pi r F(r) \tilde{L}. \quad (2.64)$$

with

$$W_\phi^r = \int_{-H}^H \langle t_\phi^r \rangle dz, \quad (2.65)$$

where W_ϕ^r is the averaged torque. The quantity $\langle t_\phi^r \rangle$ is the average value of the ϕ - r component of the stress tensor over a characteristic time scale Δt and the azimuthal angle $\Delta\phi = 2\pi$. By applying the energy-angular momentum relation $\tilde{E}_{,r} = \omega\tilde{L}_{,r}$, the flux $F(r)$ of the radiant energy over the disk can be expressed in terms of the specific energy, angular momentum, and of the angular velocity of the black hole,

$$F(r) = -\frac{\dot{M}_0}{4\pi\sqrt{-g}} \frac{\Omega_{,r}}{(\tilde{E} - \Omega\tilde{L})^2} \int_{r_{\text{ms}}}^r (\tilde{E} - \Omega\tilde{L})\tilde{L}_{,r} dr, \quad (2.66)$$

where r_{ms} is the inner edge of the thin accretion disk and is assumed to be at the radius of the marginally stable circular orbit around the slowly rotating black holes in Einstein-Æther theory. The small rotation parameter $a = J/M \ll 1$ can only affect the radius and the radiation $F(r)$ of the thin accretion disk if we consider its effects beyond the leading order. In this case, one can still use Eq.(2.57) and (2.58) to determine the radiation flux of the slowly rotating black holes.

We calculate the radiation flux $F(r)$ numerically and illustrate its behavior as a function of the radial distance for different solutions of the Einstein-Æther theory with the æther field coupling constants κ and ε . Following [37, 38], we here consider the mass accretion driven by both the Einstein-Æther black holes type I and type II with a total mass $M = 10^6 M_\odot$ with a mass accretion rate of $\dot{M}_0 = 10^{-12} M_\odot/\text{yr}$. In Fig. 2, we present that the energy flux profile $F(r)$ radiated by a thin accretion disk around the different solutions of the Einstein-Æther theory with different æther field coupling constants κ and ε . For the first solution, It is shown that the energy flux grows monotonically with decreasing the value of æther field coupling constant κ . In addition, one observes that the energy flux possesses a single maximum, which grows also monotonically with the decreasing of the value of coupling constant κ . At the same time its radial position is shifted towards the location of the horizon. The main reason is that for negative κ , the effect of the æther field coupling constant κ decreases the radius of the marginally stable orbit so that the lower limit of the integral in (2.66) becomes smaller, while for positive κ the radius of the marginally stable orbit increases so that the lower limit becomes larger. For the second type of black hole solution, we can also see the same variation law of energy flux. Comparing further with the solutions of the first type, one can easily find that the æther field coupling constant ε variation in the case of the second type of solution has a much greater impact on the energy flux than the first type of solution, although in comparison the second type of solution the coupling constant value range of the solution is much smaller. The reason for such an obvious difference is that the æther

field correction of the first type of black hole solution is on the fourth-order term of M/r , while the æther field correction of the second type of black hole solution is on the second-order term.

The accreting matter in the steady state thin disk model is supposed to be in thermodynamic equilibrium. The radiation flux $F(r)$ emitted by the thin accretion disk surface will follow Stefan-Boltzmann law. Therefore, the effective temperature of a geometrically thin black-body disk is given by

$$T_{\text{eff}}(r) = \left(\frac{F(r)}{\sigma} \right)^{1/4}, \quad (2.67)$$

where $\sigma = 5.67 \times 10^{-5} \text{ erg s}^{-1} \text{ cm}^{-2} \text{ K}^{-4}$ is the Stefan-Boltzmann constant. In Fig. 3, we display the radial profile of the effective temperature $T_{\text{eff}}(r)$ of the thin accretion disk around the different type of black hole solutions with different æther field coupling constants κ and ε . The figure of the effective temperature shows a similar behavior as that of the energy flux in Fig. 2. It is easy to see from Fig. 3 that the temperature at the fixed radius grows monotonically with the decreasing the value of κ and ε . For a positive value of the æther field coupling constant κ and ε , the accretion disk is colder than that around a Schwarzschild black hole. Similarly, the variation of the effective temperature of the thin accretion disk of the second type of black hole solution with the æther field coupling constant is much more obvious than that of the first type of solution. This is also caused by the different order of the correction term of the æther field.

Since we consider the radiation emitted by the thin accretion disk surface as a perfect black body radiation, the observed luminosity $L(\nu)$ of the thin accretion disk around the Einstein-Æther black hole type I and type II has a red-shifted black body spectrum [71, 72],

$$L(\nu) = 4\pi d^2 I(\nu) = \frac{8\pi h \cos i}{c^2} \int_{r_i}^{r_f} \int_0^{2\pi} g^3 \frac{\nu_e^3 r d\phi dr}{\exp\left(\frac{h\nu_e}{k_B T}\right) - 1}, \quad (2.68)$$

where i is the inclination angle of the thin accretion disk around the Einstein-Æther spacetime, d is the distance between the observer and the center of the thin accretion disk, r_i and r_f are the inner and outer radii of the disc, h is the Planck constant, ν_e is the emission frequency in the local rest frame of the emitter, $I(\nu)$ is the Planck distribution, k_B is the Boltzmann constant, and g is the redshift factor

$$g = \frac{\nu}{\nu_e} = \frac{k_\mu u_o^\mu}{k_\mu u_e^\mu}, \quad (2.69)$$

where ν is the radiation frequency in the local rest frame of the distant observer, $u_o^\mu = (1, 0, 0, 0)$ is the 4-velocity of the observer, and $u_e^\mu = (u_e^t, 0, 0, \Omega u_e^t)$ is the 4-velocity of the emitter. With the normalization condition, we can write the u_e^t as

$$u_e^t = \frac{1}{\sqrt{-g_{tt} - 2g_{t\phi}\Omega - g_{\phi\phi}\Omega^2}}. \quad (2.70)$$

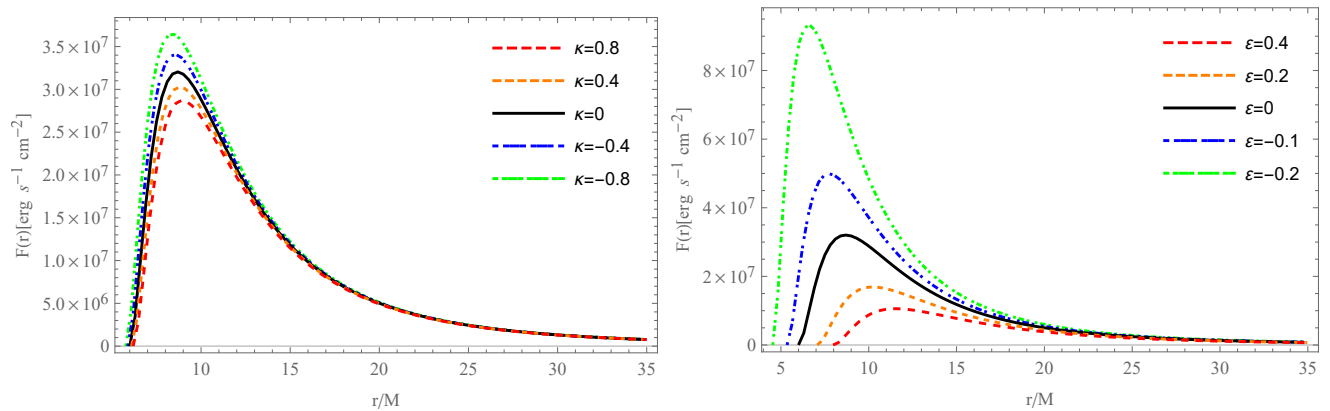


FIG. 2. Dependence of the radiated energy flux over the thin accretion disk on the radial distance for different values of the æther field coupling constant κ (left panel) for the first solution and ε (right panel) for the second one. Here the mass of the black hole and the mass accretion rate are set to be $10^6 M_\odot$ and $10^{-12} M_\odot/\text{yr}$, respectively. And we only considered $Q = 0$, the neutral black hole case.

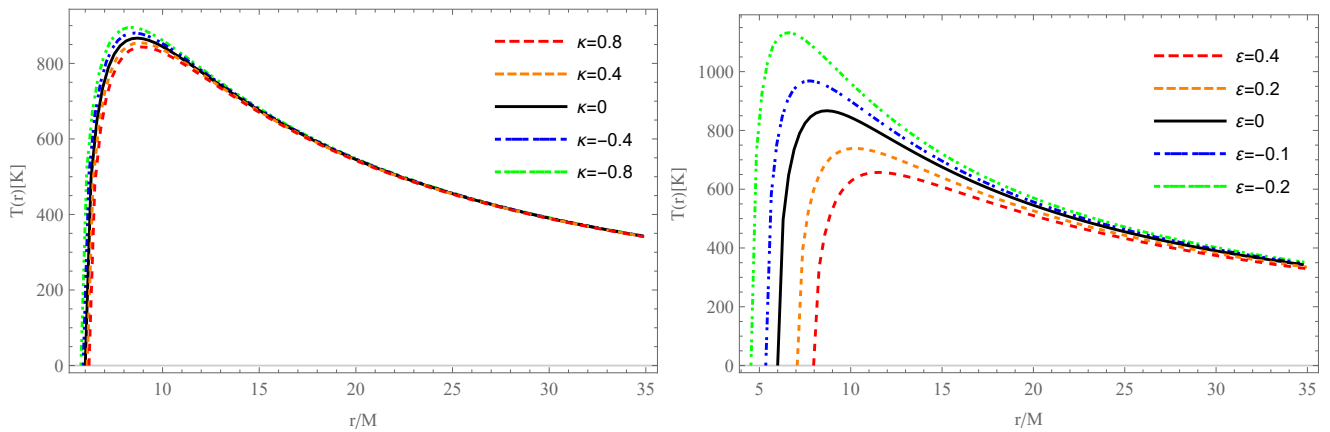


FIG. 3. The temperature profile of the thin accretion disk around the Einstein-Æther black hole for different values of the æther field coupling constant κ (left panel) for the first solution and ε (right panel) for the second one. Here the mass of the black hole and the mass accretion rate are set to be $10^6 M_\odot$ and $10^{-12} M_\odot/\text{yr}$, respectively. And we only considered $Q = 0$, the neutral black hole case.

According to the t - and ϕ -component of a photon's four momentum are conserved quantities in any static spherically symmetric spacetime, we can obtain the quantity

$$\frac{k_\phi}{k_t} = r \sin i \sin \phi, \quad (2.71)$$

then the redshift factor can be computed to be

$$g = \frac{\sqrt{-g_{tt} - 2g_{t\phi}\Omega - g_{\phi\phi}\Omega^2}}{1 + \Omega r \sin i \sin \phi}. \quad (2.72)$$

This way, we can take the relativistic effects of Doppler boost, gravitational redshift, and frame dragging into account with g . Since the flux over the disk surface vanishes at $r \rightarrow +\infty$ for asymptotically flat geometry, in this paper, we can take $r_i = r_{\text{ms}}$ and $r_f = +\infty$.

To illustrate the effect of the æther field term in the emission spectrum, we calculate the radiation spectrum $\nu L(\nu)$ numerically and display its behavior as a function of the observed frequency ν for different type of solutions

with different values of the æther field coupling constant κ and ε in Fig. 4. For negative κ and ε , it is shown that the decreasing values of κ and ε produce greater maximal amplitude of the disk emission spectrum as compared to the standard Schwarzschild case, while for positive κ and ε , it produces a smaller maximal amplitude. From these figures, one also observes that the cut-off frequencies of the emission spectra increases for the negative κ and ε) and decreases for positive κ and ε , from the value corresponding to the standard Schwarzschild black hole. Also due to the different order of the correction term of the æther field, the change of the æther field coupling constant of the second type of solution has a much greater influence on the radiation luminosity of the accretion disk than that of the solution of the first type.

At last, let us consider the accretion efficiency of the Einstein-Æther black hole, which is defined as the ratio of the rate of the radiation of energy of photons escaping from the disk surface to infinity and the rate at which

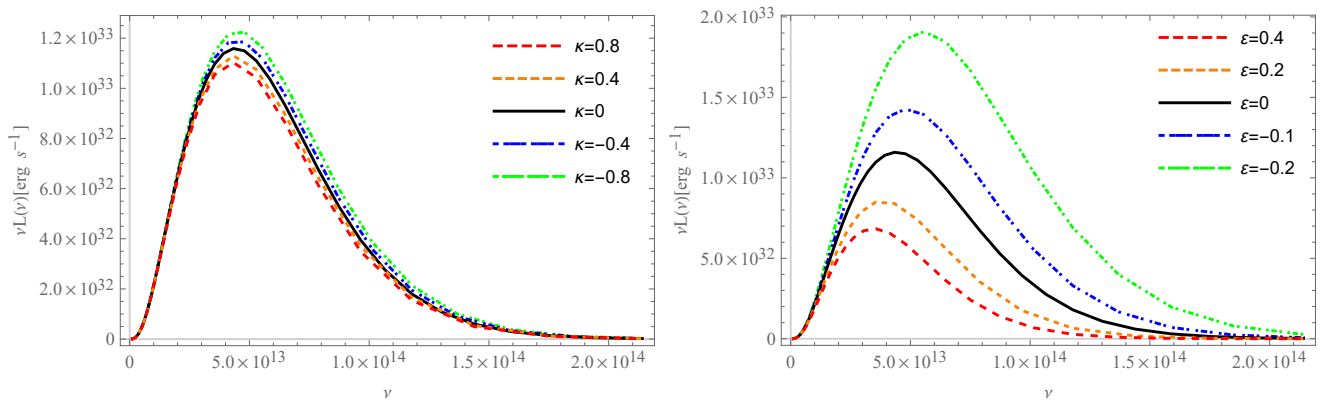


FIG. 4. The emission spectrum profile for the thin accretion disk around the Einstein-Æther black hole for different values of the æther field coupling constant κ (left panel) for the first solution and ε (right panel) for the second one. Here the mass of the black hole and the mass accretion rate are set to be $10^6 M_\odot$ and $10^{-12} M_\odot/\text{yr}$, respectively. And we only considered $Q = 0$, the neutral black hole case.

mass-energy is transported to the black hole [15, 16]. If all the emitted photons can escape to infinity, one can find that the efficiency η is related to the specific energy of the moving particle in the disk measured at the marginally stable orbit by

$$\eta = 1 - \tilde{E}_{\text{ms}}. \quad (2.73)$$

The dependence of the accretion efficiency η on the æther field coupling constant κ and ε is plotted in Fig. 5. It shows that the accretion efficiency η decreases with the increasing values of coupling constant κ for the first type of solution and ε for the second type of solution. This indicates that the accretion of matter in two types of the Einstein-Æther black hole is more efficient for the negative κ and ε and lesser efficient for the positive κ and ε than that in the Schwarzschild black hole. Therefore, the two types of Einstein-Æther black hole with negative æther field coupling constant κ and ε can provide a more efficient engine for transforming the energy of accreting matter into electromagnetic radiation than that with a positive value of κ and ε .

V. IMAGES OF THE SLOWLY ROTATING BLACK HOLES WITH ACCRETION DISK

In this section, we investigated the physical model of radiation of the thin accretion disk consisting of particles moving on circular equatorial orbits around the two types of Einstein-Æther black holes, and studied its image as seen by a distant observer. For this purpose, we construct accretion disk images for these black holes with numerical ray-tracing techniques discussed in [77]. For the ray-tracing geometry, we define the set of Cartesian coordinates (X_i, Y_i) on the image plane such that the Y -axis is along the same fiducial plane and the X -axis is perpendicular to it. We then convert the coordinates

(X, Y) of a photon that reaches the image plane to the coordinates (r, θ, ϕ) in the spherical-polar system used for the metric with the relations

$$r = \sqrt{D^2 + X^2 + Y^2}, \quad (2.74)$$

$$\cos \theta = \frac{D \cos \theta + Y \sin \theta}{r}, \quad (2.75)$$

$$\tan \phi = \frac{X}{D \sin \theta - Y \cos \theta}. \quad (2.76)$$

The photons that contribute to the image of the compact object are those with 3-momenta that are perpendicular to the image plane. This orthogonality condition uniquely specifies the momentum vector of a photon with the above coordinates, according to the relation

$$k^r \equiv \frac{dr}{d\lambda} = \frac{D}{r}, \quad (2.77)$$

$$k^\theta \equiv \frac{d\theta}{d\lambda} = \frac{-\cos \theta + \frac{D}{r^2}(D \cos \theta + Y \sin \theta)}{\sqrt{r^2 - (D \cos \theta + Y \sin \theta)^2}}, \quad (2.78)$$

$$k^\phi \equiv \frac{d\phi}{d\lambda} = \frac{-X \sin \theta}{(D \sin \theta - Y \cos \theta)^2 + X^2}. \quad (2.79)$$

With these relations, we can integrate the geodesic equations backward in time from any detection point $(X_0, Y_0, 0)$ in the image plane of the distant observer to the emission point in the disk:

$$\frac{d^2 x^\mu}{d\lambda^2} + \Gamma_{\nu\rho}^\mu \frac{dx^\nu}{d\lambda} \frac{dy^\rho}{d\lambda} = 0 \quad (2.80)$$

where λ is an affine parameter. In the numerical algorithm, we integrate geodesic equations using a Runge-Kutta integrator, which is integrated in the ode45 command of the Matlab.

According to the fact that accretion disk radiation emission is observed to follow a power law, we assume the local source intensity of the radiation emitted by the disk is

$$I_\nu(\nu, \mu, r) \propto \frac{1}{r^n} \frac{w(\mu)}{\nu(\Gamma - 1)}, \quad (2.81)$$

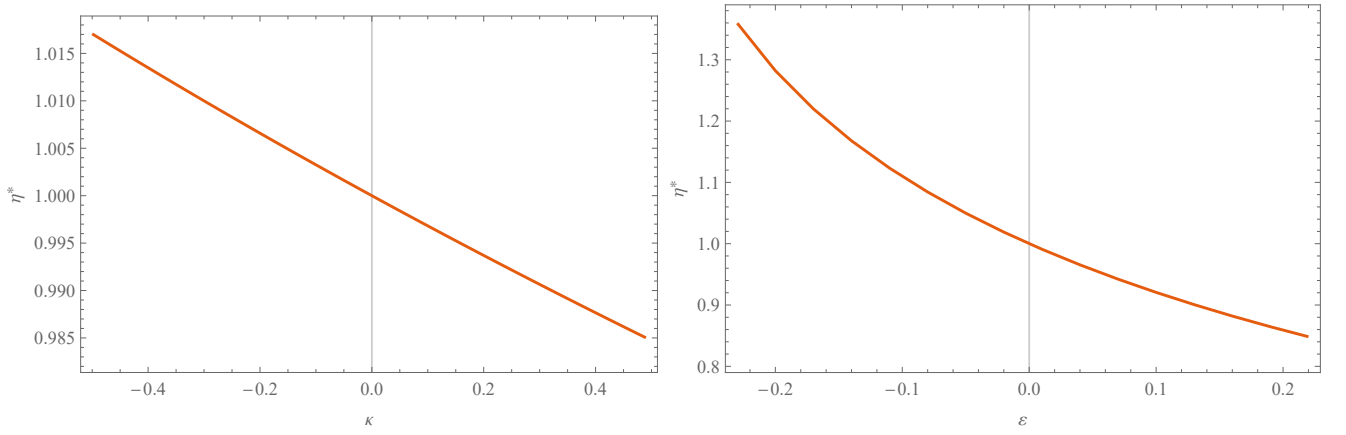


FIG. 5. The specific accretion efficiency $\eta^* = \eta/\eta_{Sch}$ of the Einstein-Æther black hole as a function of the æther field coupling constant κ (left panel) for the first solution and ε (right panel) for the second one. Here we only considered $Q = 0$, the neutral black hole case.

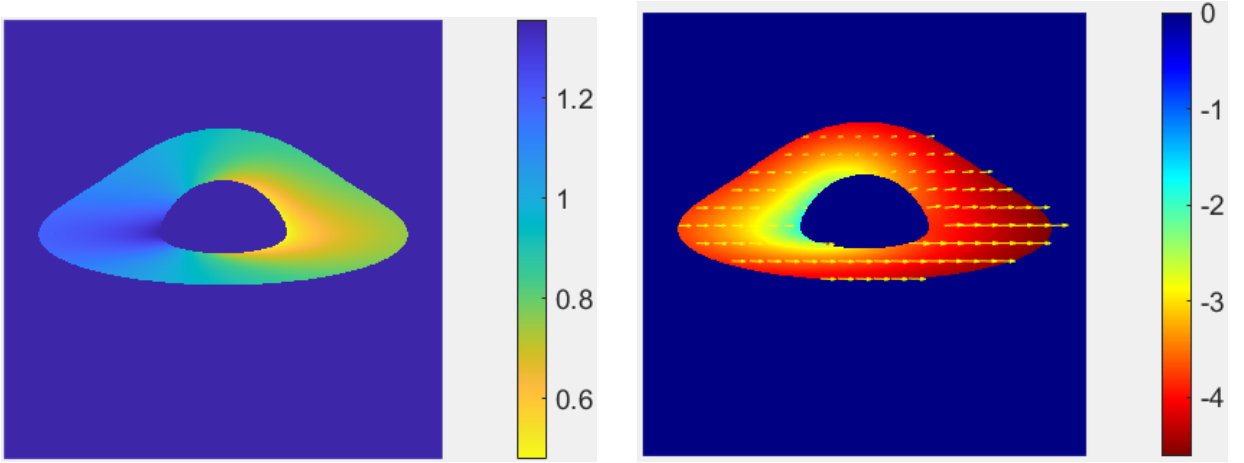


FIG. 6. Ray-traced redshifted image (left panel) and intensity and polarization profiles (right panel) of a lensed accretion disk around the Schwarzschild black hole, which corresponding to the case of $\kappa = 0$ for the first solution or $\varepsilon = 0$ for the second solution. We present the images for inclination angle $i = 75^\circ$. See the text for more details.

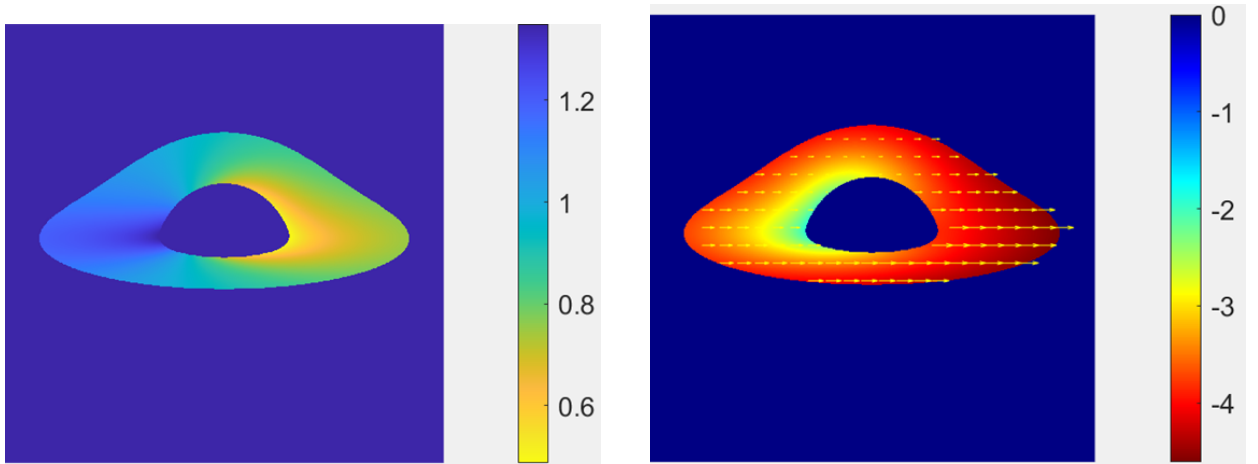


FIG. 7. Ray-traced redshifted image (left panel) and intensity and polarization profiles (right panel) of a lensed accretion disk around the first type neutral Einstein-Æther black hole. We present the images for inclination angle $i = 75^\circ$ and coupling constant $\kappa = 0.6$. See the text for more details.

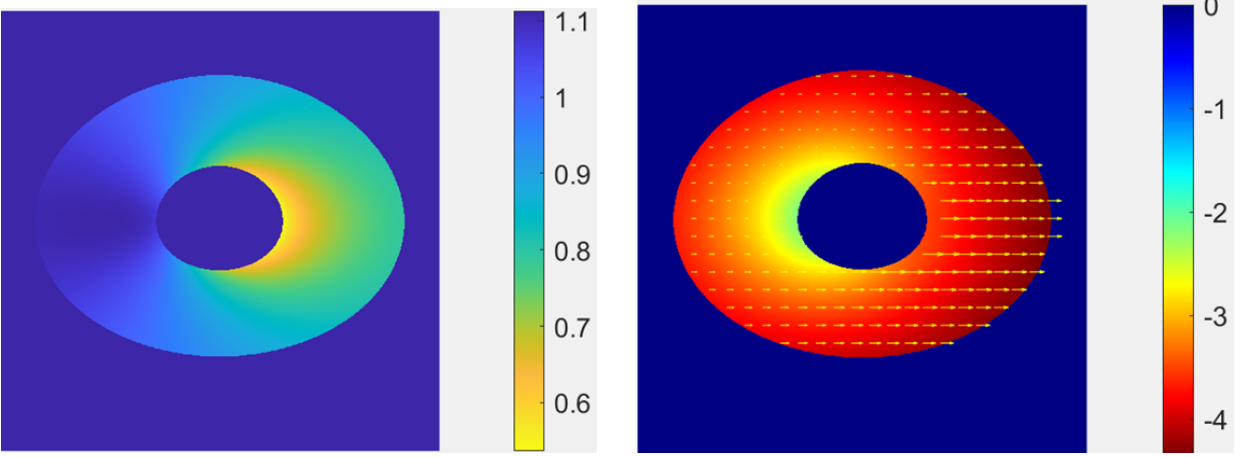


FIG. 8. Ray-traced redshifted image (left panel) and intensity and polarization profiles (right panel) of a lensed accretion disk around the first type neutral Einstein-Æther black hole. We present the images for inclination angle $i = 45^\circ$ and coupling constant $\kappa = 0.6$. See the text for more details.

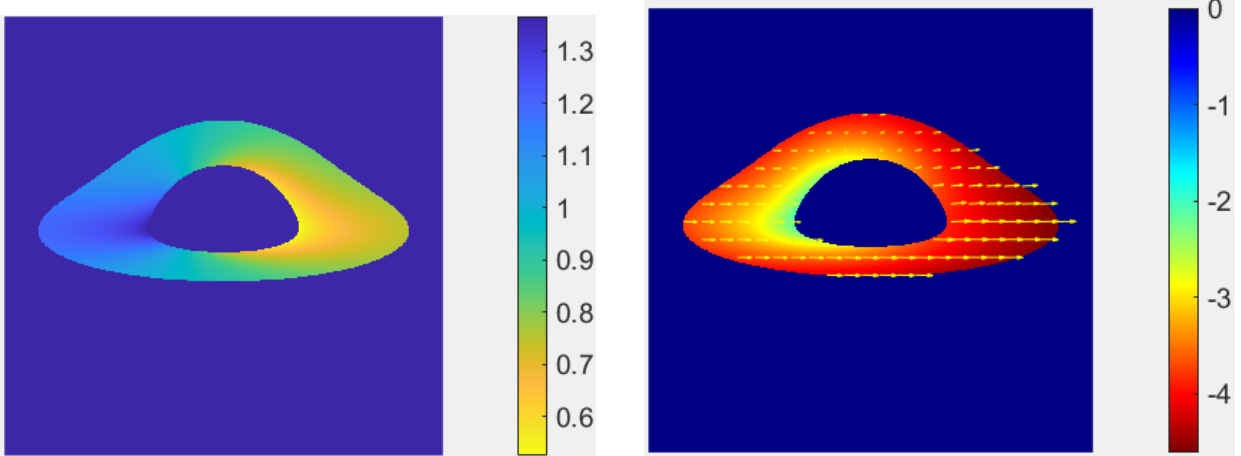


FIG. 9. Ray-traced redshifted image (left panel) and intensity and polarization profiles (right panel) of a lensed accretion disk around the second type of neutral Einstein-Æther black hole. We present the images for inclination angle $i = 75^\circ$ and coupling constant $\epsilon = 0.60$. See the text for more details.

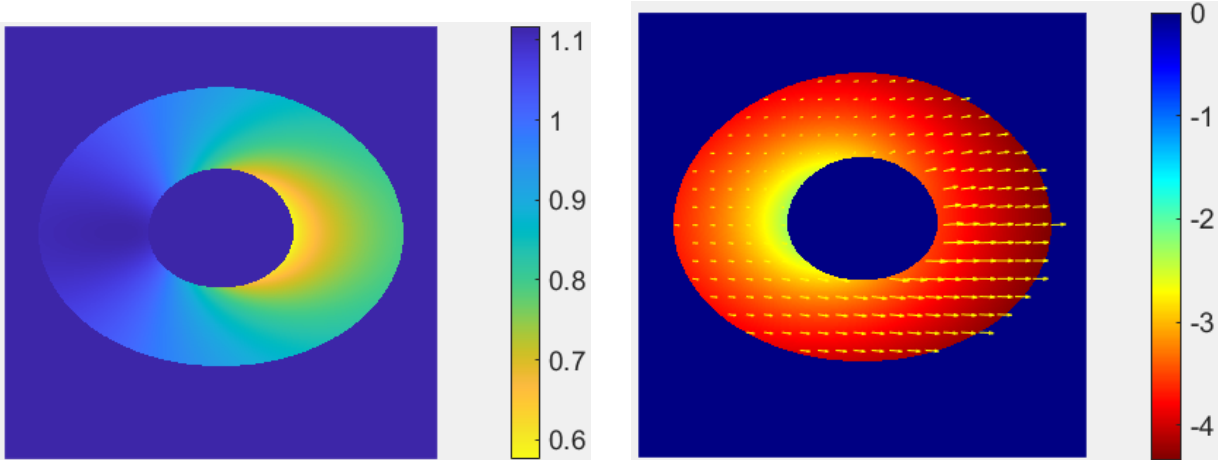


FIG. 10. Ray-traced redshifted image (left panel) and intensity and polarization profiles (right panel) of a lensed accretion disk around the second type of neutral Einstein-Æther black hole. We present the images for inclination angle $i = 45^\circ$ and coupling constant $\epsilon = 0.60$. See the text for more details.

where ν is the photon frequency in the rest frame of the gas, μ is the cosine between the photon's 4 momentum and the upward disk normal measured by the comoving observer, $w(\mu)$ is the angular-dependence of the intensity profile, Γ is a photon index and n represent the radial steepness of the intensity profile.

In addition, considering a well-known fact that a photon's polarization vector is parallel transported along the photon's geodesic and its plane of polarization is rotated as the photon passes the rotating black hole, which is called gravitational Faraday rotation, the radiation from the disk becomes partially polarized. Another factor affecting polarization is the Thomson scattering of photons off free electrons in the dense atmosphere of the disk, the degree of polarization depends on the angle i between the normal to the disk surface and the direction of propagation of the radiation photon, ranging from 0 ($i = 0^\circ$, photon direction parallel to the normal to the disk) to about 12% ($i = 90^\circ$, photon direction orthogonal to the normal to the disk). See the references [78, 79] for more details.

In Figure 6 and 7, we plot the ray-traced redshifted image of a lensed accretion disk (left panel) as well as the intensity and polarization profile (right panel) of an accretion disk around the first solution of the Einstein-Æther theory observed at inclination angle 75° but for different values $\kappa = 0$ and $\kappa = 0.6$. The former actually corresponds to the image of the thin accretion disk of the Schwarzschild black hole, which serves as a comparison for us to discuss the effects of the æther field. Figure 8 is similar to Figure 7, but for inclination angle $i = 45^\circ$. Figures 9, 10 are the same panel of graphs as Figure 7, 8, but corresponds to the thin accretion disk in the second Einstein-Æther spacetime which coupling constant takes the value $\varepsilon = 0.6$. For the ray-traced redshifted image, its color bar represents the degree of redshift of light emitted from the thin accretion disk. And for the intensity and polarization profile map, the color bar describes the intensity of radiation on the accretion disk, in addition, the arrows in the figure represent the polarization of the radiation light, and the length and direction of the arrows indicate the size and direction of the polarization, respectively.

As we all known, astrophysical black holes, whether stellar mass or supermassive, generally have strong gravitational lensing. It changes both the shape and the intensity profile of the disk significantly. The intensity is strongly concentrated in a small region (in dark red) near the black hole and to the left of the accretion disk (where the source is approaching the observer). The hat-like structure shown in the figures 6 - 9 are formed by bending the flat structure of the accretion disk due to the gravitational lensing effect of the black hole.

As we can see from the these figures, the ray-traced redshifted images and intensity and polarization profile of the thin accretion disk around both the type I and type II Einstein-Æther black holes resemble closely the Schwarzschild case. In spite of we choose an

Einstein-Æther spacetime with a value of the æther field coupling constant with maximally deviating from the Schwarzschild solution, only slight quantitative differences are present. For the first Einstein-Æther black hole solution, one can see that it is very little different from the Schwarzschild black hole case. Of course, this is also very easy to understand, for this solution correction to Schwarzschild space-time is on the fourth-order term. So for the space-time structure that is slightly farther away from the black hole, it is very difficult to see how it is different from the space-time of the Schwarzschild black hole.

For the second type of the Einstein-Æther solution, the most interesting point is that the magnification of the coupling constant has a significant impact on the disk central shadow area of the accretion disk, which is particularly evident in Figures 6 and 9, the disk central shadow area of the accretion disk increases gradually with the increase of the coupling constant ε . This result is completely consistent with the conclusions discussed by the authors in [34]. The central shadow area of the accretion disk corresponds to the shadow region of the black hole, which changes with the change of the æther field parameters. From Figures 6 and 7, 6 and 9, we can see that the coupling constants κ and ε has a very limited effect on the redshift distribution of radiated light emitted from the accretion disk. In contrast, the inclination angle has a more obvious effect on the shape of both redshifted image and intensity and polarization profile, as can be seen from figures 7 and 8 as well as figures 9 and 10.

On the other hand, we know that the magnification and direction of radiation polarization can change significantly since the gravitational Faraday rotation. This effect is more significant for source regions closer to the black hole where the observed polarization angle χ can be positive or negative (depending on the actual source location). Since what we use here is the static, spherically symmetric Einstein-Æther black hole solution, the æther field has no significant contribution to the gravitational Faraday rotational effect of light around the black hole, resulting in the æther field having no effect on the magnification and direction of polarization. However, as we can see from Figure 7 and 8, 9 and 10, the magnification increases with inclination angles and is more significant for steeper profiles. And for moderate to high inclination angles, the emission is strongly focused in a small region with a low degree of polarization.

VI. CONCLUSION AND DISCUSSION

In this paper, we study the physical properties of a thin accretion disk around two types of the black hole solutions in Einstein-Æther theory. The physical quantities of the thin accretion disk, such as the energy flux, temperature profile, electromagnetic emission spectrum profiles, and the accretion efficiency have been analyzed in detail for the two types of the black hole solutions. The

effects of the æther field coupling constant κ for the first solution and ε for the second solution in Einstein-Æther theory on these physical quantities have been explicitly obtained. For the first type of the black hole solution, it is shown that with the increases of the parameter κ , energy flux, temperature distribution, and electromagnetic spectrum of the disk all decreases. For the second type of solution, it is shown that with the increases of the parameter ε , energy flux, temperature distribution, and electromagnetic spectrum of the disk all decreases as the first black hole solution case, however, the variation of these physical quantities with the æther field coupling constant is much larger than that of the first type of black hole solution. The main reason for this kind of behaviors is that the correction of the first type of black hole solution to space-time is on the fourth-order term of M/r , and the impact on the physical properties of the surface of the accretion disk is much smaller than that of the second type of black hole solution corrected by the æther field on the second-order term.

In addition, we also show that the accretion efficiency decreases as the growth of the coupling constant κ for the first solution and ε for the second solution. Our results indicate that the thin accretion disk around the black hole in Einstein-Æther theory is hotter, more luminosity, and more efficient than that around a Schwarzschild black hole with the same mass for the first type of Einstein-Æther black hole with a negative κ and the second type of solution with a negative ε , while it is cooler, less luminosity, and less efficient for a positive κ and a positive ε . Similarly, since the different order of the correction term of the æther field, the variation range and amplitude of the accretion rate of the second type of black hole with the æther field coupling constant is also much larger than that of the first type of black hole.

Then we made the image simulation for the thin accretion disk around the two types of Einstein-Æther black holes. In this part we observe no qualitative distinction in the appearance for both the ray-traced redshifted and intensity and polarization profile of the thin accretion disk around the two types of the Einstein-Æther black holes and the Schwarzschild black hole. Only small quantitative differences are present in the disk size and the maximum of the radiation flux. We found that the æther field has a certain impact on the disk surface area of the accretion disk, the disk surface area of the accretion disk

increases gradually with the increase of the coupling constant ε for the second type of the solution. For the first type of black hole, it is difficult to see any obvious changes from the image simulation, although our parameter values are as large as possible. Moreover, for the intensity and polarization profile image, we find that the observed polarized intensity in the bright region is stronger than that in the darker region. It is also noted that the effect of æther field on the observed polarized vector is weak in general and the stronger effect of æther appears in the bright region close to black hole in the image plane. These features in the polarized image could help us to understand black hole shadow, thin accretion disk and the coupling between photon and æther field. We describe in detail the physical mechanism for the formation of the accretion disk image showing that the phenomenon is expected also for other spacetimes possessing the same properties of the photon dynamics.

With the above main results, it is of interest to constrain the black hole parameters, including the angular momentum and the æther field coupling constant κ and ε , by using the observation spectra of the X-ray binaries. For example, by using the continuum-fitting method [71] or quasi-periodic oscillations [73], one is able to measure the angular momentum of the stellar-mass black holes and constrain the deviations from Kerr metric by using X-ray data from black hole binaries. On the other hand, we aim at investigating the observable features of the two types of the Einstein-Æther black holes, which are not present for Schwarzschild black holes and could serve as an experimental test for distinguishing the two types of black holes.

ACKNOWLEDGEMENTS

This work is supported in part by the Zhejiang Provincial Natural Science Foundation of China under Grant No. LR21A050001 and LY20A050002, the National Key Research and Development Program of China Grant No.2020YFC2201503, the National Natural Science Foundation of China under Grant No. 11675143, and the Fundamental Research Funds for the Provincial Universities of Zhejiang in China under Grant No. RF-A2019015.

-
- [1] B. P. Abbott *et al.* “Observation of Gravitational Waves from a Binary Black Hole Merger,” *Phys. Rev. Lett.* **116**, 061102 (2016) [arXiv:1602.03837 [gr-qc]]; “Tests of General Relativity with GW150914,” *Phys. Rev. Lett.* **116**, 221101 (2016) [arXiv:1602.03841 [gr-qc]].
- [2] K. Akiyama *et al.* [Event Horizon Telescope Collaboration], “First M87 Event Horizon Telescope Results. I. The Shadow of the Supermassive Black Hole,” *Astrophys. J.* **875**, L1 (2019).
- [3] K. Akiyama *et al.* [Event Horizon Telescope Collaboration], “First M87 Event Horizon Telescope Results. II. Array and Instrumentation,” *Astrophys. J.* **875**, no. 1, L2 (2019) [arXiv:1906.11239 [astro-ph.IM]].
- [4] K. Akiyama *et al.* [Event Horizon Telescope Collaboration], “First M87 Event Horizon Telescope Results. III. Data Processing and Calibration,” *Astrophys. J.* **875**, no. 1, L3 (2019) [arXiv:1906.11240 [astro-ph.GA]].

- [5] K. Akiyama *et al.* [Event Horizon Telescope Collaboration], “First M87 Event Horizon Telescope Results. IV. Imaging the Central Supermassive Black Hole,” *Astrophys. J.* **875**, no. 1, L4 (2019) [arXiv:1906.11241 [astro-ph.GA]].
- [6] K. Akiyama *et al.* [Event Horizon Telescope Collaboration], “First M87 Event Horizon Telescope Results. V. Physical Origin of the Asymmetric Ring,” *Astrophys. J.* **875**, no. 1, L5 (2019) [arXiv:1906.11242 [astro-ph.GA]].
- [7] K. Akiyama *et al.* [Event Horizon Telescope Collaboration], “First M87 Event Horizon Telescope Results. VI. The Shadow and Mass of the Central Black Hole,” *Astrophys. J.* **875**, L6 (2019).
- [8] J. Frank, A. King, and D. Raine, *Accretion Power in Astrophysics*, 3rd ed. (Cambridge University Press, 2002).
- [9] F. Yuan and R. Narayan, “Hot Accretion Flows Around Black Holes,” *Annu. Rev. Astron. Astrophys.* **52**, 529 (2014).
- [10] S. Nampalliwar and C. Bambi, “Accreting Black Holes,” arXiv: 1810.07041 [astro-ph].
- [11] A. M. Hughes, A. Beasley, and C. Carilli, “Next Generation Very Large Array: Centimeter Radio Astronomy in the 2020s,” IAU General Assembly **22**, 2255106 (2015).
- [12] G. H. Sanders, “The Thirty Meter Telescope (TMT): An International Observatory,” *Journal of Astrophysics and Astronomy* **34**, 81 (2013).
- [13] C. Goddi *et al.*, “BlackHoleCam: Fundamental physics of the galactic center,” *Int. J. Mod. Phys. D* **26**, 1730001 (2016).
- [14] N.I.Shakura, R.A.Sunyaev, “Black holes in binary systems. Observational appearance.,” *Astron. Astrophys* **24**, 33(1973).
- [15] I. D. Novikov and K. S. Thorne, in *Black Holes*, edited by C.DeWitt and B. DeWitt (Gordon and Breach, New York,1973).
- [16] D. N. Page and K. S. Thorne, “Disk-accretion onto a black hole. Time-averaged structure of accretion disk,” *Astrophys.J.* **191**, 499 (1974).
- [17] P. Hořava, “Quantum gravity at a Lifshitz point,” *Phys. Rev. D* **79**, 084008 (2009).
- [18] D. Garfinkle and T. Jacobson, “A Positive-Energy Theorem for Einstein-Æther and Hořava Gravity”, *Phys. Rev. Lett.* **107**, 191102 (2011).
- [19] T. Zhu, F. W. Shu, Q. Wu and A. Wang, “General covariant Horava-Lifshitz gravity without projectability condition and its applications to cosmology,” *Phys. Rev. D* **85**, 044053 (2012); T. Zhu, Q. Wu, A. Wang and F. W. Shu, “U(1) symmetry and elimination of spin-0 gravitons in Horava-Lifshitz gravity without the projectability condition,” *Phys. Rev. D* **84**, 101502 (2011).
- [20] A. Wang, “Hořava gravity at a Lifshitz point: A progress report,” *Int. J. Mod. Phys. D* **26**, 1730014 (2017).
- [21] T. Jacobson, D. Mattingly, “Gravity with a dynamical preferred frame,” *Phys. Rev. D* **64**, 024028 (2001).
- [22] C. Eling, T. Jacobson, D. Mattingly, “Einstein-Aether Theory,” arXiv:gr-qc/0410001.
- [23] T. Jacobson, Einstein-aether gravity: a status report, arXiv: 0801.1547 [gr-qc].
- [24] B. Li, D. F. Mota, J. D. Barrow, Detecting a Lorentz-violating field in cosmology, *Phys. Rev. D* **77**, 024032 (2008).
- [25] R. A. Battye, F. Pace, D. Trinh, Cosmological perturbation theory in generalized Einstein-Aether models, *Phys. Rev. D* **96**, 064041 (2017).
- [26] T. Jacobson and D. Mattingly, “Gravity with a dynamical preferred frame,” *Phys. Rev. D* **64**, 024028 (2001).
- [27] C. Ding, A. Wang, and X. Wang, “Charged Einstein-aether black holes and Smarr formula,” *Phys. Rev. D* **92**, 084055 (2015).
- [28] C. Eling and T. Jacobson, “Black Holes in Einstein-Aether Theory,” *Class. Quant. Grav.* **23**, 5643 (2006).
- [29] Chao Zhang, Xiang Zhao, Kai Lin, Shaojun Zhang, Wen Zhao, and Anzhong Wang, “Spherically symmetric static black holes in Einstein-aether theory,” *Phys. Rev. D* **102**, 064043, arXiv:2004.06155 [gr-qc].
- [30] Jacob Oost, Shinji Mukohyama, Anzhong Wang, “Spherically symmetric exact vacuum solutions in Einstein-aether theory,” arXiv:2106.09044 [gr-qc].
- [31] R. A. Konoplya and A. Zhidenko, “Perturbations and quasi-normal modes of black holes in Einstein-Æther theory,” *Phys. Lett. B* **644**, 186 (2007).
- [32] R. A. Konoplya and A. Zhidenko, “Gravitational spectrum of black holes in the Einstein-Aether theory,” *Phys. Lett. B* **648**, 236 (2007).
- [33] A. Wang, “Stationary axisymmetric and slowly rotating spacetimes in Horava-lifshitz gravity,” *Phys. Rev. Lett.* **110**, 091101 (2013).
- [34] Tao Zhu, Qiang Wu, Mubasher Jamil, and Kimet Jusufi “Shadows and deflection angle of charged and slowly rotating black holes in Einstein-Æther theory,” *Phys. Rev. D* **100**, 044055 (2019).
- [35] Mohaddese Heydari-fard, Malihe Heydari-Fard and Hamid Reza Sepangi, “Thin accretion disks and charged rotating dilaton black holes,” arXiv:2004.05552 [gr-qc].
- [36] Tiberiu Harko, Zoltán Kovács, and Francisco S. N. Lobo, “Thin accretion disks in stationary axisymmetric worm-hole spacetimes,” *Phys. Rev. D*, **79**, 064001.
- [37] Songbai Chen, Jiliang Jing, “Thin accretion disk around a Kaluza-Klein black hole with squashed horizons,” *Phys. Let. B* **704**, 641 (2011).
- [38] Songbai Chen, Jiliang Jing, “Properties of a thin accretion disk around a rotating non-Kerr black hole,” *Phys. Let. B* **711**, 81 (2012).
- [39] Changqing Liu, Chikun Ding, Jiliang Jing, “Thin accretion disk around a rotating Kerr-like black hole in Einstein-bumblebee gravity model,” arXiv:1910.13259 [gr-qc].
- [40] Z. Zhang, S. Chen, X. Qin and J. Jing, “Polarized image of a Schwarzschild black hole with a thin accretion disk as photon couples to Weyl tensor,” *Eur. Phys. J. C* **81**, no.11, 991 (2021), [arXiv:2106.07981 [gr-qc]].
- [41] M. A. Abramowicz and P. Chris Fragile, “Foundations of black hole accretion disk theory,” *Living Rev. Relativity* **16**, 1(2013).
- [42] Shokoufe Faraji and Eva Hackmann, “Thin accretion disk around the distorted Schwarzschild black hole,” *Phys. Rev. D* **101**, 023002.
- [43] P. Joshi, D. Malafarina, and R. Narayan, “Distinguishing black holes from naked singularities through their accretion disc properties,” *Classical Quantum Gravity* **31**, 015002(2014).
- [44] Z. Kovács and T. Harko, “Can accretion disk properties observationally distinguish black holes from naked singularities?” *Phys. Rev. D* **82**, 124047 (2010).
- [45] D. F. Torres, “Accretion disc onto a static non-baryonic compact object,” *Nucl. Phys. B* **626**, 377 (2002).

- [46] V. L. Fish, K. Akiyama, K. L. Bouman, A. A. Chael, M. D. Johnson, S. S. Doeleman, L. Blackburn, J. Wardle, and W. Freeman (Event Horizon Telescope Collaboration), “Observing and imaging active galactic nuclei with the event horizon,” [telescope](#), *Galaxies* **4**, 54 (2016).
- [47] T. Müller and J. Frauendiener, “Interactive visualization of a thin disc around a Schwarzschild black hole,” *Eur. J. Phys.* **33**, 955 (2012).
- [48] A. Chowdhury, M. Patil, D. Malafarina, and P. Joshi, “Circular geodesics and accretion disks in the Janis-Newman-Winicour and gamma metric spacetimes,” *Phys. Rev. D* **85**, 104031 (2012).
- [49] Z. Kovács, K. S. Cheng, and T. Harko, “Thin accretion discs around neutron and quark stars,” *Astron. Astrophys.* **500**, 621(2009).
- [50] T. Harko, Z. Kovács, and F. S. N. Lobo, “Can accretion disk properties distinguish gravastars from black holes?” *Classical Quantum Gravity* **26**, 215006 (2009).
- [51] B. Dänilä, T. Harko, and Z. Kovács, “Thin accretion disks around cold Bose-Einstein condensate stars,” *Eur. Phys. J. C* **75**, 203 (2015).
- [52] C. S. J. Pun, Z. Kovács, and T. Harko, “Thin accretion disks in f(R) modified gravity models,” *Phys. Rev. D* **78**, 024043 (2008).
- [53] D. Pérez, G. E. Romero, and S. E. Perez Bergliaffa, “Accretion disks around black holes in modified strong gravity,” *Astron. Astrophys.* **551**, A4 (2013).
- [54] G. Gylchev, P. Nedkova, T. Vetsov, and S. Yazadjiev, “Image of the Janis-Newman-Winicour naked singularity with a thin accretion disk,” *Phys. Rev. D* **100**, 024055 (2019).
- [55] T. Harko, Z. Kovács, and F. S. N. Lobo, “Thin accretion disk signatures of slowly rotating black holes in Horava gravity,” *Classical Quantum Gravity* **28**, 165001 (2011).
- [56] M. Heydari-Fard, “Black hole accretion disks in brane gravity via a confining potential,” *Classical Quantum Gravity* **27**, 235004 (2010).
- [57] T. Harko, Z. Kovács, and F. S. N. Lobo, “Thin accretion disk signatures in dynamical Chern-Simons-modified gravity,” *Classical Quantum Gravity* **27**, 105010 (2010).
- [58] D. Pérez, F. G. Lopez Armengol, and G. E. Romero, “Accretion disks around black holes in scalar-tensor-vector gravity,” *Phys. Rev. D* **95**, 104047 (2017).
- [59] R. K. Karimov, R. N. Izmailov, A. Bhattacharya, and K. K. Nandi, “Accretion disks around the Gibbons-MaedaGarfinkle-Horowitz-Strominger charged black holes,” *Eur. Phys. J. C* **78**, 788 (2018).
- [60] G. Lodato, “Self-gravitating accretion discs,” *Nuovo Cimento Rivista Serie* **30**, 293 (2007).
- [61] Indrani Banerjee, Sumanta Chakraborty, Soumitra Sen-Gupta, “Excavating black hole continuum spectrum: Possible signatures of scalar hairs and of higher dimensions,” *Phys.Rev.D* **96** (2017) **8**, 084035.
- [62] Indrani Banerjee, Sumanta Chakraborty, Soumitra Sen-Gupta, “Decoding signatures of extra dimensions and estimating spin of quasars from the continuum spectrum,” *Phys. Rev. D* **100**, 044045.
- [63] M.U. Farooq, A.K. Ahmed, R.-J. Yang, and M. Jamil, “Accretion on High Derivative Asymptotically Safe Black Holes,” *Chin. Phys. C* **44**, 065102 (2020); A. K. Ahmed1, U. Camci, and M. Jamil, “Accretion on Reissner-Nordström-(anti)-de Sitter black hole with global monopole,” *Class. Quantum Grav.* **33** (2016) 215012; A. K. Ahmed, M. Azreg-Ainou, M. Faizal, and M. Jamil, “Cyclic and heteroclinic flows near general static spherically symmetric black holes,” *Eur. Phys. J. C* **76**, 280 (2016).
- [64] Cheng Liu, Tao Zhu, Qiang Wu, “Thin accretion disk around a four-dimensional Einstein-Gauss-Bonnet black hole,” *Chinese Phys. C* **45** 015105.
- [65] B. Z. Foster, “Radiation damping in Einstein-aether theory,” *Phys. Rev. D* **73**, 104012 (2006).
- [66] D. Garfinkle, C. Eling, and T. Jacobson, “Numerical simulations of gravitational collapse in Einstein-aether theory,” *Phys. Rev. D* **76**, 024003 (2007).
- [67] S. M. Carroll and E. A. Lim, “Lorentz-violating vector fields slow the universe down,” *Phys. Rev. D* **70**, 123525 (2004).
- [68] J. B. Hartle and K. S. Thorne, “Slowly Rotating Relativistic Stars. II. Models for Neutron Stars and Supermassive Stars,” *Astrophys. J.* **153**, 807 (1968).
- [69] E. Barausse, T. P. Sotiriou, I. Vega, “Slowly Rotating Black Holes in Einstein-æther Theory,” *Phys. Rev. D* **93**, 044044 (2016).
- [70] J. Oost, S. Mukohyama and A. Wang, “Constraints on Einstein-aether theory after GW170817,” *Phys. Rev. D* **97**, no.12, 124023 (2018) doi:10.1103/PhysRevD.97.124023 [arXiv:1802.04303 [gr-qc]].
- [71] Cosimo Bambi and Enrico Barausse, “Constraining the quadrupole moment of stellar-mass black-hole candidates with the continuum fitting method,” *Astrophys.J.* **731** (2011) 121.
- [72] Cosimo Bambi and Enrico Barausse, “Erratum: ‘Constraining the quadrupole moment of stellar-mass black-hole candidates with the continuum fitting method’,” **2011, ApJ 731, 121**.
- [73] Cosimo Bambi, “Testing the nature of the black hole candidate in GRO J1655-40 with the relativistic precession model,” *Eur. Phys. J. C* **75**, 162 (2015).
- [74] B. P. Abbott et. al. (LIGO Scientific Collaboration and Virgo Collaboration), “GW170817: Observation of Gravitational Waves from a Binary Neutron Star Inspiral,” *Phys. Rev. Lett.* **119**, 161101 (2017).
- [75] B. P. Abbott et. al. (LIGO Scientific Collaboration, Virgo Collaboration, Fermi Gamma-Ray Burst Monitor, and INTEGRAL), “Gravitational Waves and Gamma-Rays from a Binary Neutron Star Merger: GW170817 and GRB 170817A,” *Astrophys. J. Lett.* **848**, L13 (2017).
- [76] T. Jacobson and D. Mattingly, “Einstein-aether waves,” *Phys. Rev. D* **70**, 024003 (2004).
- [77] Bin Chen, Ronald Kantowski, Xinyu Dai, Eddie Baron, and Prasad Maddumage, “ALGORITHMS AND PROGRAMS FOR STRONG GRAVITATIONAL LENSING IN KERR SPACE-TIME INCLUDING POLARIZATION”, *ApJS* **218** 4(2015).
- [78] L.X. Li, R. Narayan, J.E. McClintock, “Inferring the Inclination of a Black Hole Accretion Disk from Observations of its Polarized Continuum Radiation”, *Astrophys. J.* **691**, 847(2009).
- [79] Jeremy D. Schnittman and Julian H. Krolik, “X-ray Polarization from Accreting Black Holes: II. The Thermal State”, *Astrophys. J.* **701**, 1175 (2009).